

# Entanglement-enhanced matter-wave interferometry in a high-finesse cavity

James Thompson (✉ [jkt@jila.colorado.edu](mailto:jkt@jila.colorado.edu))

JILA and University of Colorado Boulder

Graham Greve

<https://orcid.org/0000-0001-7253-2880>

Chengyi Luo

JILA and University of Colorado Boulder

Baochen Wu

JILA and University of Colorado Boulder

---

## Physical Sciences - Article

**Keywords:** cavity-QED entanglement, matter-wave interferometry, high-finesse cavity

**Posted Date:** November 24th, 2021

**DOI:** <https://doi.org/10.21203/rs.3.rs-1021592/v1>

**License:** © ⓘ This work is licensed under a Creative Commons Attribution 4.0 International License.

[Read Full License](#)

---

**Version of Record:** A version of this preprint was published at Nature on October 19th, 2022. See the published version at <https://doi.org/10.1038/s41586-022-05197-9>.

# Entanglement-enhanced matter-wave interferometry in a high-finesse cavity

Graham P. Greve<sup>1\*</sup>, Chengyi Luo<sup>1\*</sup>, Baochen Wu<sup>1</sup>, James K. Thompson<sup>1†</sup>

26 October 2021

Entanglement is a fundamental resource that allows quantum sensors to surpass the standard quantum limit set by the quantum collapse of independent atoms. Collective cavity-QED systems have succeeded in generating large amounts<sup>1;2</sup> of directly observed entanglement involving the *internal* degrees of freedom of laser-cooled atomic ensembles<sup>1–12</sup>. Here we demonstrate cavity-QED entanglement of *external* degrees of freedom to realize a matter-wave interferometer of 700 atoms in which each individual atom falls freely under gravity and simultaneously traverses two paths through space while also entangled with the other atoms. We demonstrate both quantum non-demolition measurements and cavity-mediated spin interactions for generating squeezed momentum states with directly observed metrological gain  $3.4^{+1.1}_{-0.9}$  dB and  $2.5^{+0.6}_{-0.6}$  dB below the standard quantum limit respectively. An entangled state is for the first time successfully injected into a Mach-Zehnder light-pulse interferometer with  $1.7^{+0.5}_{-0.5}$  dB of directly observed metrological enhancement. These results open a new path for combining particle delocalization and entanglement for inertial sensors<sup>13;14</sup>, searches for new physics, particles, and fields<sup>15–21</sup>, future advanced gravitational wave detectors<sup>22–24</sup>, and accessing beyond mean-field quantum many-body physics<sup>25–29</sup>.

Light-pulse matter-wave interferometers exploit the quantized momentum kick given to atoms during absorption and emission of light in order to split atomic wavepackets so that they traverse distinct spatial paths at the same time. Additional momentum kicks then return the atoms to the same point in space to interfere the two matter-wave packets. Such matter-wave interferometers are exquisitely precise and accurate quantum sensors for a vast range of applications including inertial sensing and navigation<sup>13;14</sup>, searching for dark matter<sup>19;21</sup> and dark energy<sup>15;18</sup>, determination of fundamental constants and the most precise test of a physical theory to date<sup>17;20</sup>, geodesy, geophysics and mineral and hydrocarbon exploration<sup>30</sup>, exploring general relativity with quantum probes<sup>16;31;32</sup>, and detecting gravitational waves<sup>22–24</sup>.

The key to the precision of these devices is the encoding of information in the phase  $\phi$  that appears in the superposition of the two quantum trajectories within the interferometer. This phase must be estimated from quantum measurements to extract the desired information. For  $N$  atoms, the phase estimation is fundamentally limited by the independent quantum collapse of each atom to an rms angular uncertainty  $\Delta\theta_{\text{SQL}} = 1/\sqrt{N}$  rad known as the standard quantum limit (SQL)<sup>33</sup>. Reducing this fundamental quantum source of imprecision would provide a new resource that can be exploited to directly enhance measurement precision, bandwidth, and accuracy or operate at reduced size.

Here, we demonstrate for the first time the generation and injection of quantum entanglement into a light-pulse matter-wave interferometer<sup>34;35</sup> with a direct observation of a reduction in the phase noise below the standard quantum limit. We thus simultaneously combine two of the most striking features of quantum mechanics, the concept that a particle can appear to be in two places

at once and entanglement between distinct particles. This work is also a harbinger of a future in which quantum many-body simulations using degenerate gases in cavities<sup>25–28</sup> will explore beyond mean-field physics by directly modifying and probing quantum fluctuations, or the quantum measurement process itself induces phase transitions<sup>29</sup>.

Quantum entanglement between the atoms allows the atoms to conspire together to reduce their total quantum noise relative to their total signal during the phase estimation process<sup>36;37</sup>. Such entanglement has been generated between atoms and ions using direct collisional<sup>38–44</sup> or Coulomb<sup>45;46</sup> interactions, with applications to entangled spatial interferometry in trapped geometries<sup>38;44</sup> and mapping of internal entanglement onto momentum states<sup>47</sup>.

We demonstrate for the first time, the realization of cavity-QED entanglement generation between the external momentum states of different atoms using two distinct approaches that both rely on the strong collective coupling between the atoms and an optical cavity. In the first approach, we realize cavity-enhanced quantum non-demolition measurements<sup>1–4</sup> to essentially measure and subtract out the quantum noise. In the second approach, we utilize the cavity to mediate unitary interactions between the atoms to realize so-called one-axis twisting<sup>10–12;36;48</sup> or an all-to-all Ising interaction. Both approaches have been realized for generating as much as 18.5 dB of entanglement<sup>1;2</sup>, but only between *internal* states of atoms and with only the realization of directly observed enhancements in entangled microwave clocks<sup>8;9</sup> and magnetometers<sup>49</sup>.

Strong collective coupling to the cavity  $NC \gg 1$  is the key requirement for both approaches to generate entanglement, where  $C$  is the single particle cooperativity parameter<sup>48;50;51</sup>. Previously, an interferometer was operated in a low finesse cavity<sup>52;53</sup>, to provide power build-up, spatial mode filtering, and precise beam alignment. Here, we achieve matter-wave interferometric control<sup>34;35</sup> simultaneously with strong collective coupling

<sup>1</sup>JILA, NIST and Department of Physics, University of Colorado, Boulder, CO, USA.

\*These authors contributed equally.

†email: jkt@jila.colorado.edu

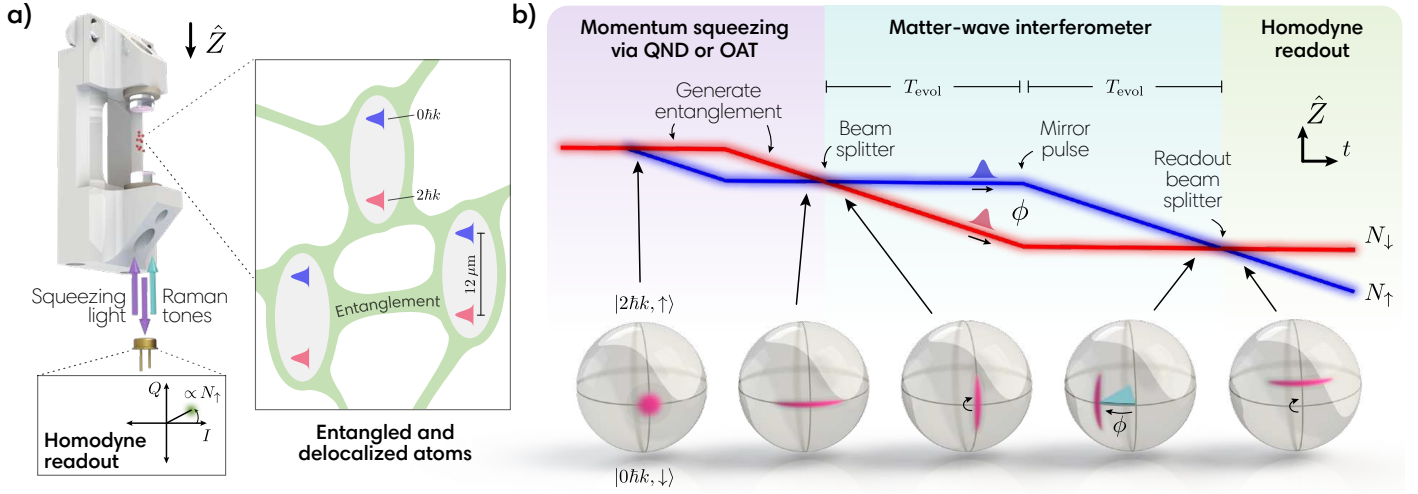


**Fig. 1 | Experimental overview.** (a) Ultracold atoms undergo guided free fall in a vertical high-finesse cavity. The atomic wavepackets are split and recombined by driving two-photon Raman transitions to provide quantized momentum kicks to the atoms. (**inset**) Intracavity atomic probe light generates entanglement between the atoms via either one-axis twisting dynamics or quantum non-demolition measurements made by detecting the reflected atomic probe field with a homodyne detector. (b) Space-time and Bloch sphere depictions of the generation and injection of the entanglement into a Mach-Zehnder matter-wave interferometer. Squeezing is first generated in the population basis, and then a Raman beam splitter pulse orients the squeezing for enhanced interferometer phase sensitivity. The two paths (red and blue) accrue a relative phase  $\phi$  over time  $2T_{\text{evol}}$ , the mirror pulse serves to reoverlap the wavepackets, and the readout beam splitter pulse creates interference that is read out as a population difference with sub-standard quantum limit sensitivity. Representative noise distributions are depicted on the Bloch sphere for various points in the interferometer.

$NC \approx 500$  by operating inside a high cavity finesse  $\mathcal{F} = 1.3 \times 10^5$  with small mode waist  $w_0 = 72 \mu\text{m}$ .

Our two-mirror cavity is vertically-oriented along  $\hat{Z}$  (Fig. 1). The cavity has a power decay rate  $\kappa = 2\pi \times 56(3)$  kHz, mirror separation  $L = 2.2$  cm, and free spectral range  $\omega_{\text{FSR}} = 2\pi \times 6.7879$  GHz (all error bars reported are  $1\sigma$  uncertainties). Rubidium atoms are loaded into a red-detuned 813 nm standing-wave intracavity lattice and laser-cooled to a radial temperature of  $0.7(3)$   $\mu\text{K}$ . The lattice is adiabatically reduced to allow the atoms to accelerate under gravity for a duration  $T_{\text{fall}}$ , guided tightly along the cavity axis by a hollow (Laguerre-Gauss  $\text{LG}_{01}$ -like) blue-detuned optical dipole guide<sup>54</sup> with thermal rms cloud radius of  $r_{\text{rms}} = 3.0(5)$   $\mu\text{m} \ll w_0$  (see Methods for additional details).

**Manipulating matter-waves.** We manipulate matter-wave wavepackets using velocity-sensitive two-photon transitions with wavelength  $\lambda = 780$  nm. The combined absorption and stimulated emission of photons imparts  $2\hbar k$  momentum kicks oriented along the cavity axis, where  $k = 2\pi/\lambda$  and  $\hbar$  is the reduced Planck constant.

For Raman transitions in which both momentum and spin states are changed, we utilize the magnetically-insensitive  $^{87}\text{Rb}$  clock states,  $|\downarrow\rangle \equiv |F=1, m_F=0\rangle$  and  $|\uparrow\rangle \equiv |F=2, m_F=0\rangle$ , separated by the hyperfine transition frequency  $\omega_{\text{HF}} \approx 2\pi \times 6.835$  GHz. The driving laser's frequency is stabilized between two  $\text{TEM}_{00}$  longitudinal modes approximately  $\Delta = 2\pi \times 85$  GHz blue-detuned of  $|\uparrow\rangle \rightarrow |e\rangle \equiv |5^2\text{P}_{3/2}, F=3\rangle$ . The cavity free spectral range is tuned such that two sidebands at  $\pm\omega_R$  are approximately  $\pm 23$  MHz from resonance with the closest  $\text{TEM}_{00}$  mode when  $2\omega_R = \omega_{\text{HF}}$ . This configuration allows enough light to nonresonantly enter the cavity for a two-photon Rabi frequency  $\Omega = 2\pi \times 10$  kHz. By injecting the Raman tones non-resonantly and with opposite detunings, we greatly suppress laser frequency

noise from being converted into phase and amplitude noise inside the cavity. Such noise manifests as noise in the Raman rotations and undesired Bragg scattering to other momentum states.

As the atoms fall under gravity inside the cavity, the relative Doppler shift for light propagating upwards versus downwards chirps linearly in time. We compensate this effect by linearly ramping the instantaneous frequency of the sidebands as  $2\omega_R = \omega_{\text{HF}} + \delta - b(t - t_{\text{vs}})$  with  $b = 2kg = 2\pi \times 25$  kHz/ms with the local acceleration due to gravity  $g = 9.8\text{m/s}^2$ ,  $\delta$  the two-photon detuning in the falling frame of reference, and  $t_{\text{vs}}$  the time at which we will apply the first  $\pi$  pulse for velocity selection described below (see Fig. 2(b) and Methods).

In Fig. 2(c), we show the initial axial velocity spectrum of the atoms as mapped out by inducing velocity-dependent spin flips. We use this same process to select atoms within a narrow range of initial velocities for coherent manipulation of matter-waves in the remainder of this work. After falling for  $T_{\text{fall}} = 15$  ms, atoms are optically-pumped to  $|\uparrow\rangle$ , and the two-photon detuning is set to  $\delta_{\text{vs}} = -400$  kHz to transfer a group of atoms to  $|\downarrow\rangle$  from the center of the axial velocity distribution<sup>55</sup>. Atoms in  $|\uparrow\rangle$  are removed by a transverse radiation pressure force. The velocity-selected atoms are returned to  $|\uparrow\rangle$  with a Raman  $\pi$  pulse and the selection process is repeated, resulting in approximately  $N_0 = 800 - 1200$  atoms in  $|\downarrow\rangle$  with rms momentum spread  $\Delta p = 0.1\hbar k$  set by choice of the two-photon Rabi frequency  $\Omega = 2\pi \times 1.4$  kHz.

In Fig. 2(d) we demonstrate the quantized nature of the momentum kicks imparted by the intracavity Raman transitions. After velocity selection, a  $\pi/2$  pulse is followed by a second Raman  $\pi$  pulse to place the atoms into a superposition of  $|0\hbar k, \downarrow\rangle$  and  $|4\hbar k, \downarrow\rangle$  in the falling frame of reference. We observe this as two distinct peaks separated in the subsequent velocity spectrum. Though not leveraged here, future interferometers might evolve in such superpositions so as to minimize systematic errors and

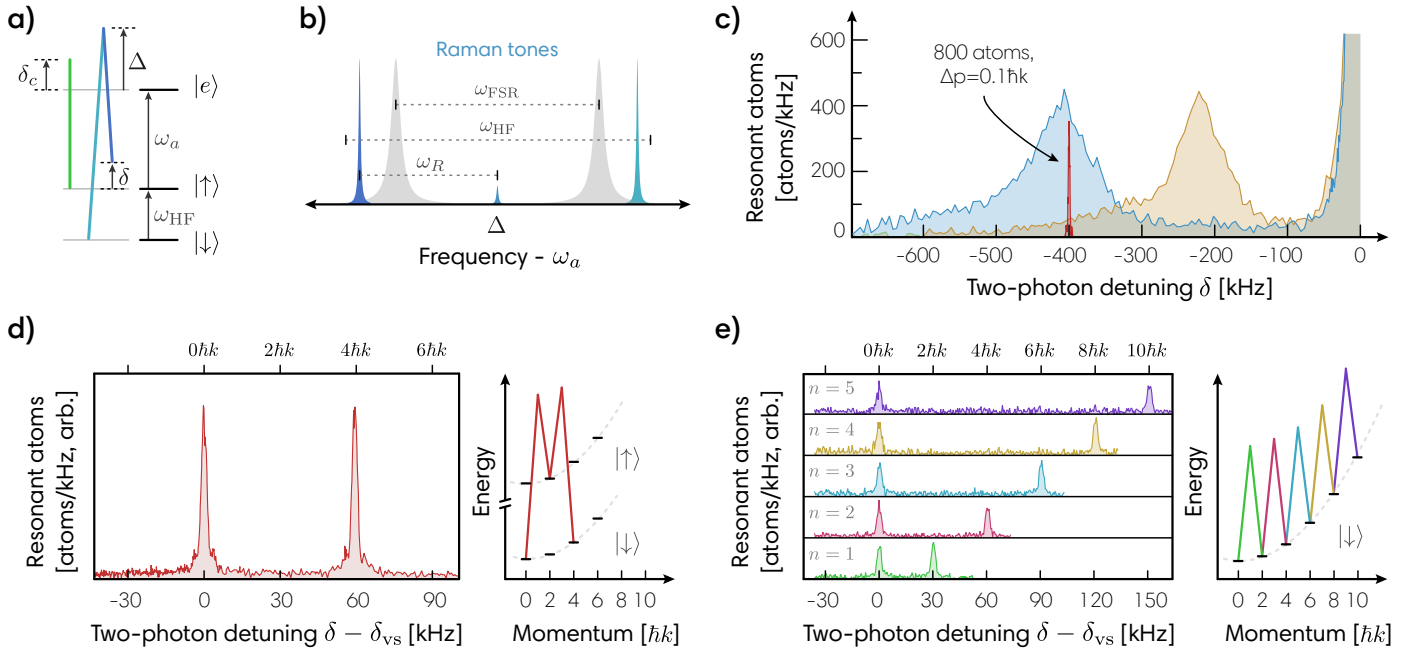


**Fig. 2 | Manipulating matter-waves in a high finesse cavity.** (a) Simplified energy-level diagram for  $^{87}\text{Rb}$ . The empty-cavity resonance (green) is detuned by  $\delta_c$  from the  $|\uparrow\rangle \rightarrow |e\rangle$  transition  $\omega_a$ . The Raman tones (blue) injected into the cavity drive a spin-changing  $|\uparrow\rangle \leftrightarrow |\downarrow\rangle$  transition with two-photon detuning  $\delta$  defined in a falling reference frame. (b) The Raman tones are derived from a laser locked between two adjacent  $\text{TEM}_{00}$  modes (grey) and modulated at  $\omega_R \sim \omega_{\text{HF}}/2$ , leaving them detuned from the cavity resonances by  $\pm 23$  MHz, close enough to resonance to allow light to enter the cavity while also sufficiently detuned to avoid strong laser FM to intracavity AM and PM conversion that would interfere with manipulating the matter-waves with a precision below the standard quantum limit. (c) Atoms are prepared in  $|\downarrow\rangle$  and allowed to fall for a duration  $T_{\text{fall}} = 7.5$  ms (orange) or 15 ms (blue). The Raman coupling is applied at a fixed detuning  $\delta$ , after which the number of atoms in  $|\uparrow\rangle$  is measured, revealing the axial velocity distribution. The full-width half-maximum of both distributions corresponds to a momentum spread of  $5\hbar k$ , too broad for interferometry. During velocity selection, a group of about 800 atoms with rms momentum spread  $\Delta p = 0.1\hbar k$  (red) are kept from the latter distribution while the rest are removed with transverse radiation pressure. (d) After velocity selection, a pair of Raman transitions can be used to place atoms into a superposition of  $|0\hbar k, \downarrow\rangle$  and  $|4\hbar k, \downarrow\rangle$ . Raman spectroscopy is used to verify the discrete velocity distribution. (e) Alternatively, Bragg transitions can be driven by adding amplitude modulation to the Raman tones. Here, a Bragg  $\pi/2$  pulse splits the wavepacket, and consecutive  $\pi$  pulses transfer additional momentum to create a superposition  $|0\hbar k, \downarrow\rangle$  and  $|2n\hbar k, \downarrow\rangle$  with the momentum difference as large as  $10\hbar k$  shown here.

dephasing due to environmental couplings to the spin degree of freedom.

Complementary to hyperfine spin-state changing Raman transitions, we also demonstrate intracavity Bragg transitions in this high finesse and high cooperativity cavity. The Bragg coupling connects states  $|n\hbar k\rangle \leftrightarrow |(n+2)\hbar k\rangle$  with no change in the spin degree of freedom, as shown in Fig. 2(e). The Bragg transitions are driven by two laser tones derived from the same laser with difference frequency  $\omega_B = \delta_{\text{vs}} - b(t - t_{\text{vs}})$ . After velocity selection, the wavepacket is coherently split by a Bragg  $\pi/2$  pulse, followed by successive  $\pi$  pulses to transfer momentum to one of the wavepacket components for a momentum difference of up to  $10\hbar k$ . Access to Bragg transitions opens the door to both large momentum transfer operations for greater sensitivity and to improved coherence times in future work.

**Squeezing on momentum states.** With the ability to manipulate matter-waves in our cavity, we turn our attention to creating entanglement between atoms that includes this *external* degree of freedom. We describe the collective state of our matter-wave interferometer using a Bloch sphere with average Bloch vector  $\vec{J} = \langle \hat{J}_x \hat{x} + \hat{J}_y \hat{y} + \hat{J}_z \hat{z} \rangle$  of length  $J \equiv |\vec{J}| \leq N_0/2$  in a fictitious coordinate space<sup>56</sup>. The collective pseudospin projection operators are defined as  $\hat{J}_z \equiv \frac{1}{2}(\hat{N}_\uparrow - \hat{N}_\downarrow)$  with collective population

projection operators  $\hat{N}_\uparrow = \sum_i^{N_0} |a\rangle_i \langle a|$  and  $\hat{N}_\downarrow = \sum_i^{N_0} |b\rangle_i \langle b|$ , and similarly for other pseudospin projections. In this work,  $|a\rangle_i = |2\hbar k, \uparrow\rangle_i$  and  $|b\rangle_i = |0\hbar k, \downarrow\rangle_i$  for the  $i$ th atom.

We use a Raman  $\pi/2$  pulse to nominally prepare all atoms in an unentangled coherent spin state  $|\psi\rangle = \prod_i^{N_0} \frac{1}{\sqrt{2}} (|a\rangle_i + |b\rangle_i)$  described by the Bloch vector  $\vec{J} = J\hat{x}$ . The quantum noise that will appear in a measurement manifests in the non-zero variance of the spin projection operators  $(\Delta J_z)^2 = \langle \hat{J}_z^2 \rangle - \langle \hat{J}_z \rangle^2 \neq 0$ , etc. and is visualized on the Bloch sphere as a quasi probability distribution of the orientation of the Bloch vector from trial to trial. It is the ratio of rms spin projection noise amplitude to the length of the Bloch vector that sets the standard quantum limit in the quantum phase estimation of the polar and azimuthal angles.

The Wineland parameter characterizes the phase enhancement of a squeezed state with phase uncertainty  $\Delta\theta$  that is certified to arise from entanglement between the atoms<sup>37</sup>

$$W = \left( \frac{\Delta\theta}{\Delta\theta_{\text{SQL}}} \right)^2. \quad (1)$$

Physically, it is the reduction in the angular noise variance of the phase estimation relative to the standard quantum limit  $\Delta\theta_{\text{SQL}} = 1/\sqrt{N}$  one would have for a pure state with a Bloch vector length  $J_c = N/2$  equal to that of the actually prepared mixed or partially decohered state absent the squeezing operation (see Methods).

We prepare squeezed momentum states through two separate cavity-based interactions: quantum non-demolition (QND) measurements<sup>1;2;50</sup> and one-axis twisting (OAT)<sup>10;36;48</sup>. In both cases, quantum noise is reduced in one spin-momentum projection at the expense of increased quantum noise along the orthogonal projection.

Population readout is achieved through collective or QND measurements of the free falling atomic samples that ideally give information about the fraction of the atoms in different spin-momentum states without revealing single-particle information<sup>50;54</sup>. The two momentum states interact differently with the optical cavity because they carry distinct spin labels. We tune a TEM<sub>00</sub> cavity mode with resonance frequency  $\omega_c$  to the blue of the  $|\uparrow\rangle \rightarrow |e\rangle$  transition  $\omega_a$  by  $\delta_c = \omega_c - \omega_a$ . After adiabatically eliminating the excited state  $|e\rangle$  and ignoring mean-field light shifts that will be spin-echoed away, the effective Hamiltonian<sup>48</sup> describing the atom-cavity QND interaction can be expressed in a rotating frame at the atomic transition frequency as

$$\hat{H}_{\text{QND}} = (\delta_c + \chi_{\text{QND}} \hat{N}_{\uparrow}) \hat{c}^{\dagger} \hat{c} \quad (2)$$

where the cavity field is described by creation and annihilation operators  $\hat{c}^{\dagger}$  and  $\hat{c}$ . The QND interaction generates entanglement between the cavity field and the collective population  $N_{\uparrow}$  in  $|\uparrow\rangle$  so that measuring the phase of the field that emerges from the cavity allows us to determine the population  $N_{\uparrow}$ . Alternatively, atoms in  $|\uparrow\rangle$  create a round trip phase shift of the intracavity light that causes the cavity resonance to shift by an amount  $\chi_{\text{QND}} = 2\pi \times 336(2)$  Hz per atom in  $|\uparrow\rangle$  at a detuning  $\delta_c = 2\pi \times 175$  MHz and accounting for interaction of the cavity mode with all excited state hyperfine levels.

The cavity frequency shift is estimated by detecting the  $Q$  quadrature of probe light reflected from the cavity input mirror as the laser frequency is swept across resonance (Fig. 3(b)). A typical measurement lasts 150  $\mu\text{s}$ . The population  $N_{\downarrow}$  of atoms in the momentum state with spin label  $|\downarrow\rangle$  is measured with the same technique after transferring the atoms to  $|\uparrow\rangle$  using a Raman  $\pi$  pulse. The Raman  $\pi$  pulse serves the additional functions of re-overlapping the wavepackets and cancelling the average light shift of the probe.

Collective QND measurements are used in creating conditional spin squeezing. The spin-momentum projection in the population basis is measured once with the pre-measurement outcome  $J_{zp} = \frac{1}{2} (N_{\uparrow} - N_{\downarrow})|_{\text{pre}}$ . The same projection is then measured a second time with the final measurement outcome labeled  $J_{zf} = \frac{1}{2} (N_{\uparrow} - N_{\downarrow})|_{\text{fin}}$ . Each final population measurement is made after first optically pumping atoms in  $|\uparrow\rangle$  to  $|F = 2, m_F = 2\rangle$  to achieve lower readout noise (estimated at more than 15 dB below the projection noise level) by using the optical cycling transition to  $|F = 3, m_F = 3\rangle$ .

If sufficiently precise, the pre-measurement localizes the state to below the initial coherent spin state level, producing a squeezed state. It can be considered a measurement of the quantum fluctuation of the orientation of the state on a given trial, and the measurement outcome can then be used to partially subtract the quantum fluctuation from the final measurement outcome by considering the difference  $J_{zd} = J_{zf} - J_{zp}$ . The quantum fluctuation is common to the two measurements, but any rotation of the state

(i.e. the signal) that occurs in between the two measurements appears only in the final measurement outcome so that one can estimate the angular displacement as  $\sin(\theta) \equiv J_{zd}/J_s$ . The length of the Bloch vector  $J_s$  after the pre-measurement has prepared a squeezed state is measured in a separate set of experiments in which a  $\pi/2$  pulse about azimuthal angle  $\phi$  is inserted between the pre- and final measurements. The length of the Bloch vector is estimated from the fringe amplitude of  $J_{zf}$  versus  $\phi$  as it is varied between 0 to  $2\pi$ . The initial length of the Bloch vector  $J_c$  needed for estimating the spectroscopic enhancement is estimated in the same manner, but without the pre-measurement applied.

Fig. 3(c) shows the spectroscopic resolution enhancement  $W$  versus the strength of the QND interaction as parameterized by  $M_i$ , the average number of incident photons that enter the cavity during each population pre-measurement window. At low  $M_i$ , the probe's vacuum noise limits the spectroscopic enhancement, while at high  $M_i$ , the spectroscopic enhancement is limited by free space scattering of the probe light that leads to a reduction in  $J_s$  and transitions to other ground states that decorrelate the pre- and final measurements. Near  $M_i = 600$ ,  $N = 1170(30)$  atoms, and  $\delta_c = 2\pi \times 175$  MHz, we achieve  $W = 0.46(11)$  or  $3.4_{-0.9}^{+1.1}$  dB of directly observed squeezing in the momentum-spin basis.

We also realize momentum-spin entanglement via cavity-mediated interactions<sup>10;48;51</sup>. The one-axis twisting (OAT) Hamiltonian<sup>36</sup>

$$\hat{H}_{\text{OAT}} = \chi_{\text{OAT}} \hat{J}_z^2 \quad (3)$$

is generated by applying a fixed frequency drive tone offset from the average dressed cavity resonance by  $\delta_p \gtrsim \kappa/2$ . Briefly, the populations in each momentum-spin state tune the cavity closer to or further from resonance with the fixed frequency drive tone, allowing more or less light into the cavity. After adiabatic elimination of the dressed cavity mode and neglecting terms that will be spin-echoed away, one finds that to first approximation,  $\hat{c}^{\dagger} \hat{c} \propto \hat{N}_{\uparrow}$ . As a result, the spin-dependent portion of the QND Hamiltonian is transformed after a spin-echo pulse into Eq. 3, a pure spin-spin Hamiltonian proportional to  $\hat{N}_{\uparrow}^2 + \hat{N}_{\downarrow}^2 = 4\hat{J}_z^2$  with the cavity mode acting as a mediator of the interaction. The unitary interactions drive shearing of the atomic quantum noise distribution with a resulting squeezed state minimum noise projection oriented at a small angle  $\alpha_0$  from  $\hat{z}$  (Fig. 4(b, inset)).

To suppress free-space scattering, it is ideal to operate at  $\delta_p = \kappa/2$ , however, we work at larger detunings. First, this reduces deleterious QND interactions (or equivalently, photon shot noise from the applied drive tone) that were neglected in the above description of the emergence of the unitary dynamics<sup>57</sup>. Secondly, this allows operation in a linearized regime even in the presence of shot-to-shot total atom number fluctuations. We empirically find an optimum detuning of  $\delta_p = 2.7 \times \kappa/2$  with  $\chi_{\text{OAT}} \approx 2\pi \times 10$  Hz.

After the OAT interaction is applied, the state is rotated using the Raman beams to couple the momentum-spin states so that the minimum noise projection is along  $\hat{z}$ . The momentum-spin populations are destructively readout out as described previously with measurement outcome labeled  $J_{zf}$ . The Bloch vector lengths  $J_s$  ( $J_c$ ) with (without) OAT squeezing are measured in the same manner as was done for the QND measurements by measuring the fringe amplitude of  $J_{zf}$  versus the azimuthal phase of a

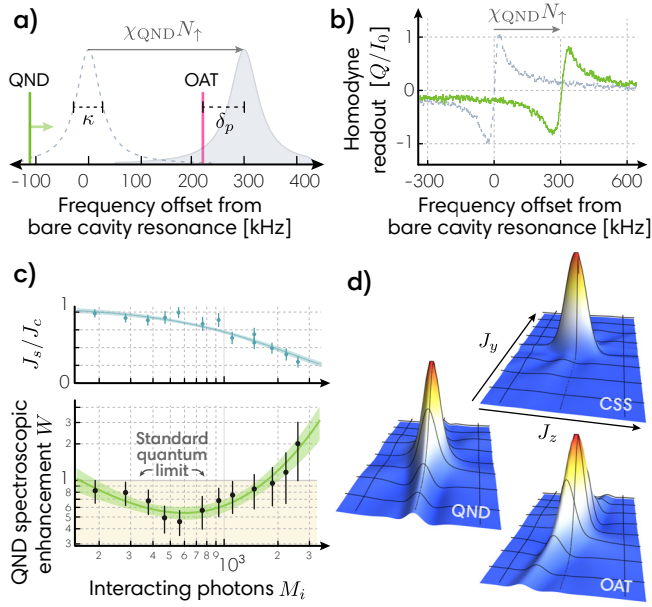


**Fig. 3 | Momentum squeezing via one-axis twisting and quantum non-demolition measurements.** (a) Probe frequency setup for OAT and QND measurements. During OAT, the laser is fixed at a detuning from cavity resonance  $\delta_p$ . QND measurements are made by sweeping the probe laser frequency over cavity resonance and detecting the  $Q$  quadrature of the reflected field. (b) QND probe sweeps measured in homodyne and normalized to the full reflected field on resonance  $I_0$ , shown for the empty cavity (gray) and for 900 atoms in  $|\uparrow\rangle$  (green). The observed frequency shift allows us to measure the collective population operator  $\hat{N}_\uparrow$  with measurement outcome  $N_\uparrow$ , without knowing which atoms are in  $|\uparrow\rangle$ . The probe is sweeping 1.5 MHz/ms and the atom-cavity detuning is  $\delta_c = 2\pi \times 175$  MHz. Free space scattering of probe light results in a slight broadening and reduced amplitude of the observed signal<sup>50</sup>. (c) QND measurements are used to pre-measure the quantum noise in the spin projection  $J_z$  and subtract it from a final measurement as in<sup>2</sup>. Increasing the number of probe photons  $M_i$  results in a more precise pre-measurement, but at too high of a photon number, free space scattering causes shortening of the Bloch vector (top) and spontaneous Raman scattering to other states. Squeezing is characterized by the spectroscopic enhancement  $W$  (bottom) which reaches an optimum below the standard quantum limit at  $M_i = 600$  photons. (d) State tomography was performed to construct the spin-momentum quasi-probability distributions in the  $J_y - J_z$  plane for a coherent spin-state (CSS), a QND-squeezed state, and an OAT-squeezed state.

$\pi/2$  rotation prior to the final readout. We achieve a directly observed spectroscopic enhancement from OAT of  $W = 0.56(8)$  or  $2.5^{+0.6}_{-0.6}$  dB. The optimal configuration was realized with  $M_i \approx 700$  photons,  $\delta_c = 2\pi \times 350$  MHz, and  $N = 730(10)$  atoms.

**Entangled matter-wave interferometry.** We now turn to injecting the prepared entangled states into a matter-wave interferometer. We use a slightly modified Mach-Zehnder Raman interferometer with  $(\pi/2 - \pi - \pi/2)$  pulse sequence to coherently separate, undo the separation, and interfere the atomic wavepackets. In analogy to an optical Mach-Zehnder interferometer, the  $\pi/2$  pulses play the role of 50/50 beam splitters at the entrance and exit of the interferometer and the  $\pi$  pulse plays the role of the mirrors that redirect the beams from the input beam splitter to the output beam splitter.

After preparing a squeezed state with OAT, a Raman beam splitter rotation orients the squeezing along  $\hat{y}$ . The spin projection  $J_y$  will change if a small signal phase  $\phi$  is applied. The ori-

enting of the squeezing is accomplished via a  $(\pi/2 + \alpha_0)$  pulse aligned to the atomic Bloch vector along  $\hat{x}$ . A relative phase accumulates between the wavepackets during a free evolution time  $T_{\text{evol}}$ , a Raman  $\pi$  “mirror” pulse is applied, followed by another free evolution time  $T_{\text{evol}}$ . Finally, a readout  $\pi/2$  pulse transfers the signal  $\phi$  and the squeezing into a displacement in the momentum-spin population basis  $\hat{z}$  with a measurement outcome  $J_{z,f}$ . The Bloch vector lengths  $J_s$  and  $J_c$  are measured in separate experiments with and without OAT applied by scanning the azimuthal phase of the final  $\pi/2$  pulse of the interferometer and measuring the fringe amplitude as before (see Fig. 4(c)).

We achieve a directly observed spectroscopic enhancement as measured by the Wineland parameter of  $1.7^{+0.5}_{-0.5}$  dB beyond the standard quantum limit with  $N = 660(15)$  atoms as shown in Fig. 4(b). We also note that the actual phase variance of the interferometer is reduced by  $3.4^{+0.9}_{-1.2}$  dB compared to with no one axis twisting, consistent with expectations from  $J_c$ .

Phase sensitivity beyond the SQL was limited to evolution times  $T_{\text{evol}} < 0.7$  ms (Fig. 4(d)). Evidence from purely microwave interferometers with no momentum states involved suggests this loss of observable squeezing was primarily due to magnetic field fluctuations in the lab that lead to added fluctuations in the azimuthal phase accrued during the interferometer evolution times. The matter-wave interferometer is sensitive to vibration noise, but the measured accelerations are not sufficient to explain the loss of directly observed entanglement (see Methods). Single-particle decoherence is also inadequate as an explanation because  $J_c$  decreased by less than 5% over these evolution times. We also observe that if the squeezed spin projection is left in the population basis  $J_z$  during the interferometer, then the squeezing persists for several milliseconds. From this, we conclude that the entangled state persists for longer than we can directly confirm because the interferometer is detecting an undesired magnetic field signal that masks the quantum noise reduction as  $T_{\text{evol}}$  increases.

In the future, the magnetic field noise can be reduced and looking further ahead, the combination of Raman and Bragg techniques demonstrated here would enable the most delicate portion of the superposition possessing the same spin label. To further improve interferometer sensitivity, the entanglement can be combined with large momentum transfer sequences, one could inject the squeezed state into a lattice interferometer to hold the atoms longer<sup>53</sup>, or prepare the entanglement in the cavity and allow the atoms to undergo free fall and subsequent fluorescence measurement readout<sup>8</sup>.

The amount of momentum squeezing could be improved with larger collective cooperativity  $NC$ . The need for velocity selection limits our final number of atoms, so higher atom density in momentum space through improved axial cooling or the use of a Bose-Einstein condensate could lead to significant improvements<sup>39; 58–60</sup>. It will also be possible to perform the entanglement generation utilizing optical cycling transitions in rubidium, strontium, and ytterbium<sup>2; 6; 12; 50; 54</sup> for which the fundamental scaling of the achievable Wineland parameter would improve to  $W \propto 1/NC$  from the current scaling  $W \propto 1/\sqrt{NC}$ .

This proof-of-principle light-pulse matter-wave interferometer paves the way for utilizing cavity-generated entanglement as a

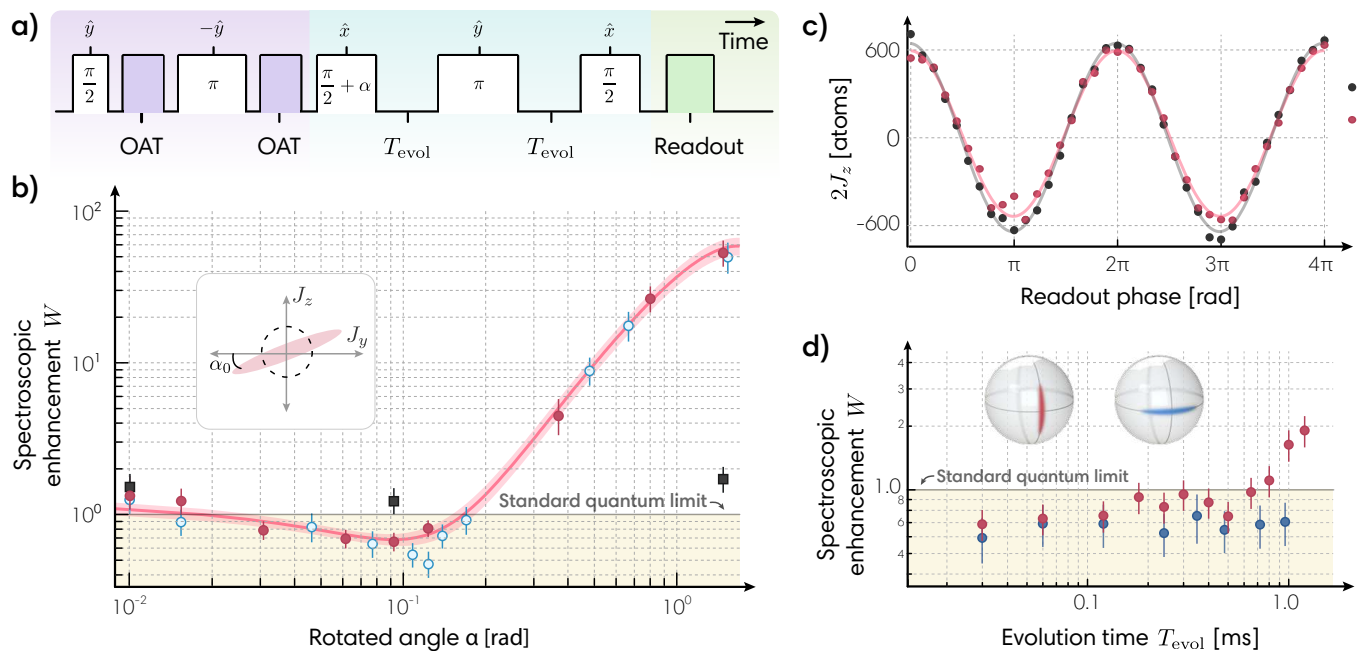


**Fig. 4 | Demonstrating sensitivity beyond the standard quantum limit.** (a) The squeezed interferometer sequence, including entanglement generation (purple), the interferometer (blue), and state readout (green). Each Raman transition (white rectangle) is labeled with magnitude (within) and axis of rotation (above). (b) The spectroscopic enhancement  $W$  is compared for three configurations: a Mach-Zehnder interferometer with OAT (red circles, sequence above), an unentangled interferometer without OAT (black squares), and OAT-squeezed states without the interferometer (blue circles). The duration of a  $\pi/2 + \alpha$  rotation is scanned to minimize the projected spin noise at  $\alpha_0$ . An ellipse is fit with 68% confidence bands to the OAT-squeezed interferometer data, giving a minimum variance of  $W = 0.68(8)$  or  $1.7^{+0.5}_{-0.5}$  dB. The interferometer here had  $T_{evol} = 0.112$  ms. (c) Interferometer contrast fringes with  $T_{evol} = 0.112$  ms shown for no squeezing  $J_c$  (black) and with squeezing  $J_s$  (red). (d) Phase sensitivity is maintained below the SQL for the squeezed interferometer (red circles, left Bloch sphere) up to  $T_{evol} = 0.7$  ms. By contrast, if the squeezed spin projection is oriented along the population basis (blue circles, right Bloch sphere), spectroscopic enhancement was seen to persist beyond  $T_{evol} = 1$  ms because this orientation is insensitive to phases accrued during the evolution time.

quantum resource, enabling the next generation of interferometers with higher precision, enhanced measurement bandwidth, higher accuracy, and smaller size. Such devices will advance the frontiers of both practical applications and discoveries in fundamental science, from particles and fields to gravitational wave detection<sup>13–18; 20–24; 30; 31; 52; 53; 58–62</sup>, and build a bridge to a future where cavity-QED-based quantum many-body simulations will move beyond mean-field physics to probe and manipulate quantum fluctuations in large ensembles of atoms<sup>25–29</sup>.

## References

- O. Hosten, N. J. Engelsen, R. Krishnakumar & M. A. Kasevich. Measurement noise 100 times lower than the quantum-projection limit using entangled atoms. *Nature* **529** no. 7587, p. 505 (2016).
- K. C. Cox, G. P. Greve, J. M. Weiner & J. K. Thompson. Deterministic Squeezed States with Collective Measurements and Feedback. *Phys. Rev. Lett.* **116**, p. 093602 (2016).
- M. H. Schleier-Smith, I. D. Leroux & V. Vuletić. States of an Ensemble of Two-Level Atoms with Reduced Quantum Uncertainty. *Phys. Rev. Lett.* **104**, p. 073604 (2010).
- Z. Chen, J. G. Bohnet, S. R. Sankar, J. Dai & J. K. Thompson. Conditional spin squeezing of a large ensemble via the vacuum Rabi splitting. *Phys. Rev. Lett.* **106** no. 13, pp. 133601–133604 (2011).
- G. Vasilakis et al. Generation of a squeezed state of an oscillator by stroboscopic back-action-evading measurement. *Nature Physics* **11** no. 5, pp. 389–392 (2015).
- J. G. Bohnet et al. Reduced spin measurement back-action for a phase sensitivity ten times beyond the standard quantum limit. *Nature Photonics* **8**, pp. 731–736 (2014).
- M.-Z. Huang et al. Self-amplifying spin measurement in a long-lived spin-squeezed state (2020). E-print.
- B. K. Malia, J. Martínez-Rincón, Y. Wu, O. Hosten & M. A. Kasevich. Free Space Ramsey Spectroscopy in Rubidium with Noise below the Quantum Projection Limit. *Phys. Rev. Lett.* **125**, p. 043202 (2020).

- I. D. Leroux, M. H. Schleier-Smith & V. Vuletić. Orientation-Dependent Entanglement Lifetime in a Squeezed Atomic Clock. *Phys. Rev. Lett.* **104**, p. 250801 (2010).
- I. D. Leroux, M. H. Schleier-Smith & V. Vuletić. Implementation of Cavity Squeezing of a Collective Atomic Spin. *Phys. Rev. Lett.* **104**, p. 073602 (2010).
- O. Hosten, R. Krishnakumar, N. J. Engelsen & M. A. Kasevich. Quantum phase magnification. *Science* **352** no. 6293, pp. 1552–1555 (2016).
- E. Pedrozo-Peñafiel et al. Entanglement on an optical atomic-clock transition. *Nature* **588** no. 7838, pp. 414–418 (2020).
- F. Riehle, T. Kisters, A. Witte, J. Helmcke & C. J. Bordé. Optical Ramsey spectroscopy in a rotating frame: Sagnac effect in a matter-wave interferometer. *Phys. Rev. Lett.* **67**, pp. 177–180 (1991).
- A. Peters, K. Y. Chung & S. Chu. Measurement of gravitational acceleration by dropping atoms. *Nature* **400** no. 6747, pp. 849–852 (1999).
- P. Hamilton et al. Atom-interferometry constraints on dark energy. *Science* **349** no. 6250, pp. 849–851 (2015).
- G. Rosi et al. Quantum test of the equivalence principle for atoms in coherent superposition of internal energy states. *Nature Communications* **8** no. 1, p. 15529 (2017).
- R. H. Parker, C. Yu, W. Zhong, B. Estey & H. Müller. Measurement of the fine-structure constant as a test of the Standard Model. *Science* **360** no. 6385, pp. 191–195 (2018).
- D. O. Sabulsky et al. Experiment to Detect Dark Energy Forces Using Atom Interferometry. *Phys. Rev. Lett.* **123**, p. 061102 (2019).
- Y. Abou El-Neaj et al. AEDGE: atomic experiment for dark matter and gravity exploration in space. *EPJ Quantum Technology* **7** no. 1, pp. 1–27 (2020).
- L. Morel, Z. Yao, P. Cladé & S. Guellati-Khélifa. Determination of the fine-structure constant with an accuracy of 81 parts per trillion. *Nature* **588** no. 7836, pp. 61–65 (2020).
- M. Abe et al. Matter-wave Atomic Gradiometer Interferometric Sensor (MAGIS-100). *Quantum Science and Technology* **6** no. 4, p. 044003 (2021).
- P. W. Graham, J. M. Hogan, M. A. Kasevich & S. Rajendran. New Method for Gravitational Wave Detection with Atomic Sensors. *Phys. Rev. Lett.* **110**, p. 171102 (2013).
- M. A. Norcia, J. R. K. Cline & J. K. Thompson. Role of atoms in atomic gravitational-wave detectors. *Phys. Rev. A* **96**, p. 042118 (2017).
- B. Canuel et al. Exploring gravity with the MIGA large scale atom interferometer. *Scientific Reports* **8** no. 1, p. 14064 (2018).

25. R. M. Kroeze, Y. Guo & B. L. Lev. Dynamical Spin-Orbit Coupling of a Quantum Gas. *Phys. Rev. Lett.* **123**, p. 160404 (2019).
26. M. Landini et al. Formation of a Spin Texture in a Quantum Gas Coupled to a Cavity. *Phys. Rev. Lett.* **120**, p. 223602 (2018).
27. H. Keßler et al. Observation of a Dissipative Time Crystal. *Phys. Rev. Lett.* **127**, p. 043602 (2021).
28. S. C. Schuster, P. Wolf, S. Ostermann, S. Slama & C. Zimmermann. Supersolid Properties of a Bose-Einstein Condensate in a Ring Resonator. *Phys. Rev. Lett.* **124**, p. 143602 (2020).
29. B. Skinner, J. Ruhman & A. Nahum. Measurement-Induced Phase Transitions in the Dynamics of Entanglement. *Phys. Rev. X* **9**, p. 031009 (2019).
30. Y. Bidel et al. Absolute marine gravimetry with matter-wave interferometry. *Nature Communications* **9**, p. 627 (2018).
31. P. Asenbaum, C. Overstreet, M. Kim, J. Curti & M. A. Kasevich. Atom-Interferometric Test of the Equivalence Principle at the  $10^{-12}$  Level. *Phys. Rev. Lett.* **125**, p. 191101 (2020).
32. P. Asenbaum et al. Phase Shift in an Atom Interferometer due to Spacetime Curvature across its Wave Function. *Phys. Rev. Lett.* **118**, p. 183602 (2017).
33. W. M. Itano et al. Quantum projection noise: Population fluctuations in two-level systems. *Phys. Rev. A* **47**, pp. 3554–3570 (1993).
34. M. Kasevich & S. Chu. Atomic interferometry using stimulated Raman transitions. *Phys. Rev. Lett.* **67**, pp. 181–184 (1991).
35. A. D. Cronin, J. Schmiedmayer & D. E. Pritchard. Optics and interferometry with atoms and molecules. *Rev. Mod. Phys.* **81**, pp. 1051–1129 (2009).
36. M. Kitagawa & M. Ueda. Squeezed spin states. *Phys. Rev. A* **47**, pp. 5138–5143 (1993).
37. D. J. Wineland, J. J. Bollinger, W. M. Itano & D. J. Heinzen. Squeezed atomic states and projection noise in spectroscopy. *Phys. Rev. A* **50**, pp. 67–88 (1994).
38. J. Esteve, C. Gross, A. Weller, S. Giovanazzi & M. K. Oberthaler. Squeezing and entanglement in a Bose-Einstein condensate. *Nature* **455** no. 7217, pp. 1216–1219 (2008).
39. C. Gross, T. Zibold, E. Nicklas, J. Estève & M. K. Oberthaler. Nonlinear atom interferometer surpasses classical precision limit. *Nature* **464** no. 7292, pp. 1165–1169 (2010).
40. R. Bücker et al. Twin-atom beams. *Nature Physics* **7** no. 8, pp. 608–611 (2011).
41. C. D. Hamley, C. S. Gerving, T. M. Hoang, E. M. Bookjans & M. S. Chapman. Spin-nematic squeezed vacuum in a quantum gas. *Nature Physics* **8** no. 4, pp. 305–308 (2012).
42. X.-Y. Luo et al. Deterministic entanglement generation from driving through quantum phase transitions. *Science* **355** no. 6325, pp. 620–623 (2017).
43. K. Lange et al. Entanglement between two spatially separated atomic modes. *Science* **360** no. 6387, pp. 416–418 (2018).
44. M. Fadel, T. Zibold, B. Décamps & P. Treutlein. Spatial entanglement patterns and Einstein-Podolsky-Rosen steering in Bose-Einstein condensates. *Science* **360** no. 6387, pp. 409–413 (2018).
45. D. Leibfried et al. Creation of a six-atom ‘Schrödinger cat’ state. *Nature* **438** no. 7068, pp. 639–642 (2005).
46. T. Monz et al. 14-Qubit Entanglement: Creation and Coherence. *Phys. Rev. Lett.* **106**, p. 130506 (2011).
47. F. Anders et al. Momentum Entanglement for Atom Interferometry. *Phys. Rev. Lett.* **127**, p. 140402 (2021).
48. M. H. Schleier-Smith, I. D. Leroux & V. Vuletić. Squeezing the collective spin of a dilute atomic ensemble by cavity feedback. *Phys. Rev. A* **81**, p. 021804 (2010).
49. B. Braverman et al. Near-Unitary Spin Squeezing in  $^{171}\text{Yb}$ . *Phys. Rev. Lett.* **122**, p. 223203 (2019).
50. Z. Chen, J. G. Bohnet, J. M. Weiner, K. C. Cox & J. K. Thompson. Cavity-aided nondemolition measurements for atom counting and spin squeezing. *Phys. Rev. A* **89**, p. 043837 (2014).
51. J. Borregaard, E. J. Davis, G. S. Bentsen, M. H. Schleier-Smith & A. S. Sørensen. One- and two-axis squeezing of atomic ensembles in optical cavities. *New Journal of Physics* **19** no. 9, p. 093021 (2017).
52. P. Hamilton et al. Atom Interferometry in an Optical Cavity. *Phys. Rev. Lett.* **114**, p. 100405 (2015).
53. V. Xu et al. Probing gravity by holding atoms for 20 seconds. *Science* **366** no. 6466, pp. 745–749 (2019).
54. K. C. Cox, G. P. Greve, B. Wu & J. K. Thompson. Spatially homogeneous entanglement for matter-wave interferometry created with time-averaged measurements. *Phys. Rev. A* **94**, p. 061601 (2016).
55. M. Kasevich et al. Atomic velocity selection using stimulated Raman transitions. *Phys. Rev. Lett.* **66**, pp. 2297–2300 (1991).
56. R. P. Feynman, F. L. Vernon Jr & R. W. Hellwarth. Geometrical representation of the Schrödinger equation for solving maser problems. *Journal of applied physics* **28** no. 1, pp. 49–52 (1957).
57. Y.-L. Zhang, C.-L. Zou, X.-B. Zou, L. Jiang & G.-C. Guo. Detuning-enhanced cavity spin squeezing. *Phys. Rev. A* **91**, p. 033625 (2015).
58. Y.-J. Wang et al. Atom Michelson Interferometer on a Chip Using a Bose-Einstein Condensate. *Phys. Rev. Lett.* **94**, p. 090405 (2005).
59. G.-B. Jo et al. Long Phase Coherence Time and Number Squeezing of Two Bose-Einstein Condensates on an Atom Chip. *Phys. Rev. Lett.* **98**, p. 030407 (2007).
60. M. Gebbe et al. Twin-lattice atom interferometry. *Nature Communications* **12** no. 1, p. 2544 (2021).
61. T. L. Gustavson, A. Landragin & M. A. Kasevich. Rotation sensing with a dual atom-interferometer Sagnac gyroscope. *Classical and Quantum Gravity* **17** no. 12, pp. 2385–2398 (2000).
62. M. Jaffe et al. Testing sub-gravitational forces on atoms from a miniature in-vacuum source mass. *Nature Physics* **13** no. 10, pp. 938–942 (2017).
63. J. Arit, K. Dholakia, L. Allen & M. J. Padgett. The production of multiringed Laguerre–Gaussian modes by computer-generated holograms. *Journal of Modern Optics* **45** no. 6, pp. 1231–1237 (1998).
64. V. Vuletić, C. Chin, A. J. Kerman & S. Chu. Degenerate Raman Sideband Cooling of Trapped Cesium Atoms at Very High Atomic Densities. *Phys. Rev. Lett.* **81**, pp. 5768–5771 (1998).
65. R. W. Tkach & A. R. Chraplyvy. Regimes of feedback effects in  $1.5\text{-}\mu\text{m}$  distributed feedback lasers. *Journal of Lightwave Technology* **4**, p. 1655 (1986).
66. Q. Lin, M. A. V. Camp, H. Zhang, B. Jelenković & V. Vuletić. Long-external-cavity distributed Bragg reflector laser with subkilohertz intrinsic linewidth. *Opt. Lett.* **37** no. 11, pp. 1989–1991 (2012).
67. M. Yamoah et al. Robust kHz-linewidth distributed Bragg reflector laser with optoelectronic feedback. *Opt. Express* **27** no. 26, pp. 37714–37720 (2019).
68. Z. Chen, J. G. Bohnet, J. M. Weiner & J. K. Thompson. A low phase noise microwave source for atomic spin squeezing experiments in  $^{87}\text{Rb}$ . *Review of Scientific Instruments* **83** no. 4, 044701.

## Methods

### Blue-detuned donut dipole guide

The blue dipole guide laser is a 760 nm interference filter ECDL locked to a reference cavity for improved long-term stability. The laser is modulated by a fiber EOM with modulation index  $\beta \approx 1.3$  at the cavity free spectral range  $\omega_{\text{FSR}}$ . By exciting adjacent longitudinal modes of the cavity with opposite spatial parity with respect to the center of the cavity, one creates an axially-uniform blue dipole guide near the center of the cavity<sup>54</sup>. The donut-mode  $\text{LG}_{01}$  profile is constructed from the  $\pm 1$ st diffraction orders of a fork-pattern phase plate<sup>63</sup>. Stress-induced birefringence of the cavity mirrors breaks cylindrical symmetry and splits the Hermite-Gaussian  $\text{HG}_{10}$  and  $\text{HG}_{01}$  modes up to  $\delta_{\text{HG}} = 2\pi \times 100 - 500$  kHz, depending on cavity piezo voltage, to be compared to the 157(5) kHz FWHM cavity linewidth for these modes. For the data presented here,  $\delta_{\text{HG}} = 2\pi \times 350$  kHz. Prior to entering the cavity, the two LG modes are sent along separate paths. One path enters a free-space EOM to generate sidebands for locking the cavity to the blue dipole guide laser. The other path passes through two AOMs with a  $\delta_{\text{HG}}$  frequency difference such that the projected HG modes combine within the cavity to approximate an  $\text{LG}_{01}$  mode's radial intensity distribution via  $\text{LG}_{01} = \text{HG}_{01} + i\text{HG}_{10}$ . Because the frequency splitting  $\delta_{\text{HG}}$  is much greater than the radial trap frequency, the atoms effectively experience the time-averaged radial trapping potential of an  $\text{LG}_{01}$  mode.

### Laser cooling

The experimental sequence is repeated every 750 ms. Each trial begins with a 2D MOT loading a 3D MOT with  $10^8$  atoms near the cavity center for approximately 0.5 s. The MOT coils are turned off, and around  $2 \times 10^5$  atoms are cooled via polarization gradient cooling to 15  $\mu\text{K}$  and loaded into an 813.5 nm red-detuned intracavity lattice with FWHM cavity linewidth 166(5) kHz. Additional radial confinement is provided by the blue dipole guide. The red lattice depth is ramped down to a depth of 80  $\mu\text{K}$  or  $250E_I$  where  $E_I$  is the recoil energy of the lattice. We then apply  $\Lambda$ -enhanced grey molasses cooling. Each of the six molasses beams has 2.5 mW and 1 cm beam waist. The light is detuned  $2\pi \times 42$  MHz blue of  $|F = 2\rangle \rightarrow |F' = 2\rangle$ . A fiber EOM generates a 100  $\mu\text{W}$  sideband for coherently forming the  $\Lambda$  system as  $|F = 1\rangle \leftrightarrow |F' = 2\rangle \leftrightarrow |F = 2\rangle$ . After 5 ms, the temperature of the ensemble is reduced to 6  $\mu\text{K}$ .

We then perform two-dimensional degenerate Raman sideband cooling (RSBC) to further cool the radial temperature to 0.7(3)  $\mu\text{K}$ <sup>64</sup>. Three RSBC beams form a triangular lattice in a plane perpendicular to the cavity axis  $\hat{Z}$ , with trapping frequency  $\omega_{\text{tri}} = 2\pi \times 75$  kHz. The blue dipole guide and red lattice continue to provide a background radial trap. The RSBC laser is blue-detuned 50 GHz from the  $|F = 1\rangle \leftrightarrow |F' = 2\rangle$  transition so that atoms are trapped at the nodes of the triangular lattice, suppressing scattering off the cooling beams. A bias magnetic field of 0.11 G along  $\hat{Z}$  is applied to match the first-order Zeeman splitting to the trap frequency  $\omega_{\text{tri}}$ . The polarizations of the three beams are twisted by  $10^\circ$  from vertical to create the Raman coupling for driving the vibrational mode transition  $|F = 1, m_F, n_{\text{tri}}\rangle \rightarrow |F = 1, m_F - 1, n_{\text{tri}} - 1\rangle$  that reduce the vi-

brational quantum number  $n_{\text{tri}}$  in the local traps. During RSBC, atoms are continuously repumped back to  $|F = 1, m_F = 1\rangle$  by a separate laser.

To improve the coupling of the atoms to the cavity we apply multiple cooling cycles each lasting 2 ms. The RSBC light is ramped on over 0.3 ms, cooling occurs for 1.2 ms, and then RSBC light is ramped off over 0.3 ms. After 225  $\mu\text{s}$ , the atoms have oscillated back to the center of the cavity, at which point we repeat the cooling cycle. After three cooling cycles, we slowly turn off the remaining red lattice and the RSBC lattice in 3 ms so that the atoms start to free fall with rms radial extent  $r_{\text{rms}} = 3.0(5) \mu\text{m}$ .

### Atomic and cavity probe lasers

To stabilize the frequencies of the Raman lasers and the atomic probe relative to the cavity, we frequency lock a separate cavity probe laser to the cavity and then perform offset frequency phase locks to this laser. The cavity probe is locked to a cavity  $\text{TEM}_{00}$  mode approximately 160 GHz to the blue of the atomic transition frequency  $\omega_a$  such that this mode is essentially unperturbed by the presence of atoms. The locking of the cavity probe to the cavity is done via a Pound-Drever-Hall lock at very low phase modulation index for a single sideband to carrier power ratio of  $10^{-4}$ . Rather than locking to the carrier, we lock to the weak sideband. This allows us to reduce the amount of power entering the cavity to only 400 pW (half from the sideband and half nonresonantly from the carrier) while still operating above the technical noise floor of the photodiode. This lock is always engaged. To allow phase locking of other lasers to the cavity probe with relative beat notes less than 2 GHz, some of the laser light is passed through a fiber EOM driven strongly at 13.6 GHz to generate very high order sidebands.

The atomic probe laser is phase-locked with an offset frequency of approximately  $13.6 \times 12 = 163.2$  GHz to the red of the cavity probe, placing it close to  $\omega_a$ . The offset phase-lock frequency is adjusted to maintain the atomic probe laser approximately  $\delta_c/2\pi + 80$  MHz blue of  $\omega_a$ . We derive three important tones from this laser: a homodyne reference beam, a path length stabilization beam used for removing path length noise and drift, and the actual atomic probe tone used for one axis twisting and QND measurements. The path length stabilization beam is passed through an EOM that is modulated at 80 MHz to create a weak sideband that will serve as the atomic probe tone. The combined path length stabilization and atomic probe tones are reflected from the cavity and detected on a single homodyne detector. The homodyne reference beam is shifted by an 80 MHz AOM to have the same frequency as the atomic probe tone. The quadrature of the atomic probe tone that we detect in homodyne is actively stabilized by adjusting the phase of the homodyne reference tone. This is achieved by detecting the phase of the path length stabilization tone appearing in the homodyne detector at 80 MHz and then holding this phase constant by feedback on the frequency of the 80 MHz AOM used to shift the homodyne reference beam.

The laser could be actively locked to the dressed resonance as  $\text{in}^2$ , or the linear part of the dispersive could be used to estimate small frequency shifts, but for this work, we sweep the atomic probe laser, and all derived beams, so that the atomic probe tone sweeps through cavity resonance resonance at 1.5 MHz/ms. Although this simplifies the experiment, it results in a 6 dB loss of

quantum efficiency for a fixed amount of free space scattering when compared to performing homodyne detection on line center. Including this loss of efficiency, the net effective quantum efficiency is approximately 10%.

The cavity probe, atomic probe and Raman lasers are DBRs with free-running linewidths of approximately 500 kHz. We use external optical feedback to narrow their linewidths<sup>65–67</sup>. A small fraction of the power from each laser is picked off and then retro-reflected back into the laser with a round trip length of 3 m in free space. The frequency of each laser is primarily determined by the length of the optical feedback path length which is stabilized using a piezo to move the retro-reflection mirror and a free-space phase modulator EOM for fast actuation with unity gain frequency of 500 kHz. By optimizing the optical feedback fraction typically between  $10^{-4}$  to  $10^{-3}$ , we achieve Lorentzian linewidths of less than 1 kHz.

### Microwave source

High fidelity Raman pulse sequences require agile control of low-phase noise microwaves. Our microwave source is based on Ref. <sup>68</sup>. A low phase noise 100 MHz crystal oscillator (Wenzel ULN 501-16843) is multiplied to 6.800 GHz using a nonlinear transmission line frequency comb generator (Picosecond Pulse Labs LPN7110-SMT). The stable 6.800 GHz is provided as the local oscillator for a single sideband modulator (Analog Devices HMC496).

The required  $I$  and  $Q$  modulation inputs to the single sideband modulator are created using three RF tones from an Analog Devices AD9959 DDS. Two RF tones are at the same frequency near 135 MHz and are 90 degrees out of phase. The phase, frequency, and amplitude of these two tones can be jumped for arbitrary rotations on the Bloch sphere, for selecting different momentum-changing transitions, velocimetry, etc. The third RF tone starts near 100 MHz but is continuously ramped in frequency at a rate  $2kg \approx 2\pi \times 25.1$  kHz/ms to match the time variation of the two-photon Doppler shift as the atoms fall under gravity. Each of the two initial RF tones are mixed with this third signal to generate tones near 35 MHz for the  $I$  and  $Q$  inputs to the single sideband modulator.

Finally, the modulator output near 6.835 GHz is divided by two using a low-noise divider (Analog Devices HMC862A) and applied to a fiber-coupled EOM to generate the desired Raman tones as the  $\pm 1$ st order sidebands. We estimate that the noise contributed by this frequency source is at least 30 dB below the SQL for 1000 atoms.

### Raman laser setup

The laser that drives the Raman transitions is detuned  $\Delta = 2\pi \times 85$  GHz blue of  $\omega_a$ . As is done for the atomic probe, the Raman laser is stabilized with respect to the cavity by an offset frequency phase lock to the cavity probe. The offset frequency is set to center the Raman laser between two adjacent longitudinal TEM<sub>00</sub> cavity modes. The two Raman tones, whose generation is described above, are symmetrically detuned from the cavity resonances by approximately  $(\omega_{\text{HF}} - \omega_{\text{FSR}})/2 = 2\pi \times 23$  MHz. With 2.5 mW of total  $\sigma^+$ -polarized light incident on the cavity, the EOM modulation index allows an observed two-photon Rabi frequency of up to  $\Omega = 2\pi \times 15$  kHz.

The Raman laser is a DBR laser with a free-running linewidth of approximately 500 kHz. We observed that the cavity converted laser frequency noise to intracavity amplitude noise near  $\delta_{\text{vs}}$  that can resonantly drive undesired Bragg transitions, leading to a loss of nearly 50% of population to other momentum states outside of the desired two-level basis for all the Raman pulses involved in the interferometer sequence combined. We note that in the symmetric detuning configuration here, the Raman transitions are first order insensitive to conversion of laser frequency noise to both AM and PM noise on the intracavity Raman tones. However, the Bragg transitions are first order sensitive because of the opposite parity of the standing wave modes being driven.

After narrowing the laser to a Lorentzian linewidth of less than 1 kHz, we found the fraction of total atoms lost out of the desired two-level manifold is less than 3(3)% for all the Raman pulses involved in the interferometer sequence combined. We also observed residual off-resonance transitions to other momentum states if the turn on and off of the Raman beams was too rapid. The fraction of atoms lost was reduced below 2(2)% by using an rf switch with 3  $\mu$ s rise-time to gate the Raman tones.

### Interpretation of the Wineland criterion

The Wineland criterion is often presented in the following form

$$W = \frac{(\Delta J_z)^2 C_i}{\Delta J_{z, \text{SQL}}^2 C_f^2}, \quad (4)$$

where the contrasts are related to Bloch vector lengths here by  $C_i \equiv 2J_c/N_0$  and  $C_f \equiv 2J_s/N_0$  for total atom number  $N_0$ . By rearranging terms, it can also be expressed in a more physically meaningful form as the ratio  $W = (\Delta\theta/\Delta\theta_{\text{SQL}})^2$  between the observed angular resolution  $\Delta\theta = \frac{\Delta J_z}{J_s}$  with entanglement and the standard quantum limit  $\Delta\theta_{\text{SQL}} = 1/\sqrt{N} \equiv 1/\sqrt{2J_c}$  for a pure state with the same Bloch vector length  $J_c$  as that of the actual mixed state when entanglement is not created.

For QND measurements, we evaluate with  $\Delta J_z = \Delta J_{z,d}$  and for OAT we evaluate with  $\Delta J_z = \Delta J_{z,f}$ , typically using 100 to 200 experimental trials. In a separate set of measurements, the size of the interferometer fringe  $2J_s$  is measured by scanning the readout  $\pi/2$  pulse azimuthal phase through  $[0, 2\pi]$ , and fitting the peak-to-peak amplitude of the fringe. To measure  $N = 2J_c$ , OAT or QND is temporarily disabled by using  $M_i = 0$ , but the window durations are left intact. The size of the interferometer fringe  $2J_c$  is then measured as before by scanning the readout  $\pi/2$  pulse azimuthal phase.

Without the introduction of QND measurements or one-axis twisting, the mixed state actually performs worse than the standard quantum limit, conceptually due to the spin noise from the dephased or decohered fraction of the atoms that contribute noise but no signal. This is why the observed improvement in the interferometer sensitivity is larger than the Wineland parameter; however, the Wineland parameter captures what fraction of the improvement can be certified to arise due to entanglement between the atoms and not due to just cancellation of spin noise alone.

### Vibration noise

Mechanical vibrations of the cavity mirrors are equivalent to a fluctuating phase reference for the atoms. A commercial vibrom-

702  
703  
704  
705  
706  
707  
708  
709  
710  
711  
712  
713  
714  
715  
716  
717  
718  
719  
720  
721  
722  
723  
724  
725  
726  
727  
728  
729  
730  
731  
732  
733  
734  
735  
736  
737  
738  
739  
740  
741  
742  
743  
744  
745  
746  
747  
748  
749  
750  
751  
752  
753

754 eter was used to measure the spectral density  $S_a(\omega)$  of accel-  
755 eration noise at a location on the optical table close to the portion  
756 that supports the vacuum chamber. In the limit of zero-duration  
757 pulses, the transfer function for a Mach-Zehnder interferometer  
758  $|T(\omega)|^2 = \frac{64k^2}{\omega^4} \sin\left(\frac{\omega T_{\text{evol}}}{2}\right)^4$  converts accelerations to an inte-  
759 grated phase noise  $\phi^2 = \int_0^\infty |T(\omega)|^2 S_a(\omega) d\omega$ . For a sequence  
760 with  $T_{\text{evol}} = 0.3$  ms, we estimate the phase noise caused by vibra-  
761 tions is 20 dB lower than the phase resolution set by the SQL of  
762 1000 atoms.

### 763 **Acknowledgements**

764 We acknowledge funding support from the National Science  
765 Foundation under Grant Numbers 1734006 (Physics Frontier  
766 Center) and OMA-2016244 (QLCI), DOE Quantum Systems Ac-  
767 celerator, NIST, and DARPA. We acknowledge helpful feedback  
768 on the manuscript from Dana Z. Anderson and Ana Maria Rey,  
769 helpful discussions with Matthew Jaffe and Nicola Poli, and laser  
770 locking development by Denton Wu.

### 771 **Author contributions**

772 G.P.G., C.L., and B.W. contributed to the building of the experi-  
773 ment, G.P.G. and C.L. conducted the experiments and data anal-  
774 ysis. J.K.T. conceived and supervised the experiments. G.P.G.,  
775 C.L., and J.K.T. wrote the manuscript. All authors discussed  
776 the experiment implementation and results and contributed to the  
777 manuscript.

### 778 **Data availability**

779 All data obtained in the study are available from the correspond-  
780 ing author upon reasonable request.

### 781 **Competing interests**

782 The authors declare no competing interests.